Breaking Material Property Trade-offs via Macrodesign of Microstructure

Qingzhong Mao, Yusheng Zhang, Jizi Liu, and Yonghao Zhao*

ACCESS | Metrics & More | Article Recommendations | SI Supporting Information

ABSTRACT: Many properties of materials are incompatible with each other or even completely exclusive. Here, we proposed a new concept in view of the trade-off paradox of material properties, which is to macrodirectionally design the microstructure of materials according to their specific service requirements to accurately use the properties of materials to the extreme. By using this concept, we successfully solved the paradox of high strength and high conductivity of copper contact wire in a high-speed train. Our concept can be used to solve the other property paradoxes of functional and structural materials.
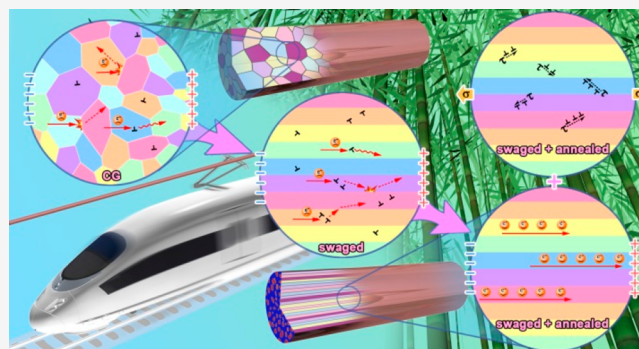
KEYWORDS: *material property paradox, macrodirectional design of microstructure, ultrafine grained copper, electrical conductivity, strength, thermal stability*

INTRODUCTION

With the rapid development of modern industry, there is an urgent need for multifunctional materials which have more than two excellent properties at the same time.[1] Unfortunately, many excellent properties of materials rarely coexist, i.e. the so-called property trade-off paradox. As a universal law of nature, such paradoxes exist widely in the important properties of structural and functional materials, such as energy and power densities of battery materials,[2] electrical conductivity and Seebeck coefficient/thermal conductivity of thermoelectric materials,[3] polarization and breakdown strength of dielectric materials,[4] magnetization and coercivity of magnetic materials,[5] reactant mobility and catalytic active sites of catalytic materials,[6] strength and ductility/conductivity/thermal stability of structural materials,[10−12] etc. (Table 1[2−12]). In the past half century, mankind has launched a tenacious and unremitting challenge to this difficult problem using emerging nanotechnology. For example, a bimodal and heterogeneous composite concept can optimize the properties more or less by combining the corresponding microstructures favorable to exclusive properties together.[10,13,14]

For the answer to the paradox of material performance, we have to look for it from the artist of nature itself. To resist transverse fracture and transport nutrients longitudinally, bamboo and other trunks have evolved a fiber structure along the longitudinal direction.[15] In the same way, shells have evolved a multilayer structure to resist vertical fracture, and teeth have evolved nanostructures on their surfaces for wear resistance.[16] Nature has skillfully and finely optimized the

Table 1. Lists of Typical Trade-offs between Conflicting Properties I and II

|	materials	property I	property II	ref
1	battery materials	energy density	power density, cycle life, safety	2
2	thermoelectric materials	electrical conductivity	Seebeck coefficient, thermal conductivity	3
3	dielectric materials	polarization	breakdown strength	4
4	permanent magnetic materials	coercivity	magnetization	5
5	catalytic materials	reactant mobility	catalytic active sites	6
6	ferroelectric/ ferromagnetic materials	ferromagnetism	ferroelectricity	7
7	optoelectronic materials	transparency	conductivity	8
8	damping materials	damping capability	elastic modulus	9
9	structural materials	strength	ductility, formability, deformability, conductivity, thermal stability	10−12
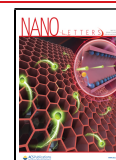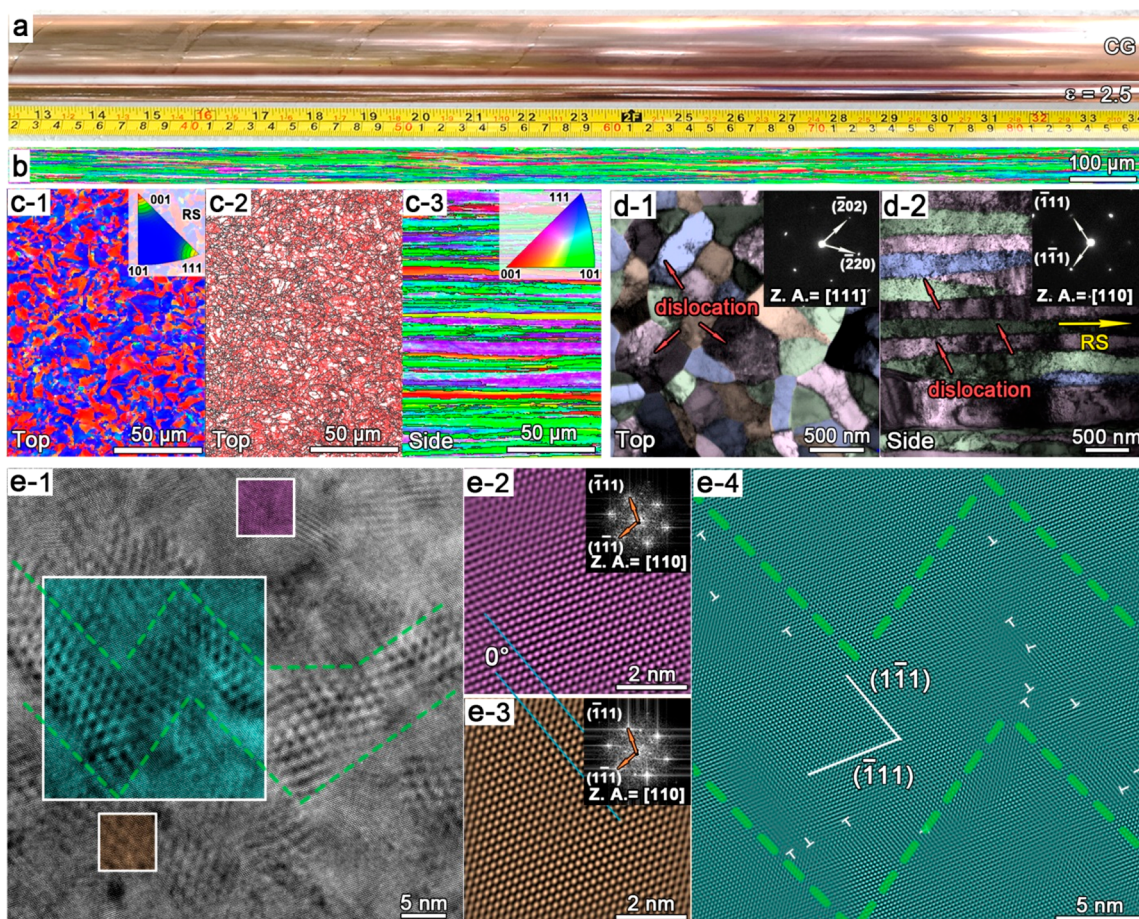
Figure 1. Microstructures of the swaged Cu with $\varepsilon = 2.5$. (a) Picture of initial CG and swaged Cu rods. (b) EBSD crystal orientation map from the side view. (c) EBSD crystal orientation maps (c-1, c-3) and GB maps (c-2) from the top (c-1, c-3) and side (c-3) views. The insets are inverse pole figures and color codes, respectively. Black and red lines in c-2 represent high-angle GBs (>15°) and low angle GBs between 2° and 15°, respectively. (d) TEM images from the top (d-1) and side (d-2) views. The insets are selected area electron diffraction (SAED) patterns. (e) High-resolution TEM image of low-angle GBs. Inverse Fourier transformation (e-4) revealed zigzag low-angle GBs formed by polygonized dislocation walls.

microstructures of biological materials according to their specific service requirements, thus evolving their multiple functions. Compared with biological materials, the current man-made materials are still simple. For example, from the atomic structure, most of the artificial materials are single-phase; from the performance point of view, most of them are isotropic, which results in the material properties not being fully utilized because the specific service parts are always macroscopic and directional. Here, we propose a new concept that the microstructure of materials should be macrodirectionally designed according to their specific working conditions. By using this concept, the paradox of high strength and high conductivity of the copper contact wire in a high-speed train was successfully solved along axial direction.

RESULTS

Macrodirectional Preparation and Microstructures of Ultrafine Grained Cu. We utilized rotary swaging (RS) to prepare a Cu wire with fiber texture and overlong ultrafine grains aligned along the wire axis. Specifically, we deformed an annealed high-purity Cu rod (99.98%, Table S1 and Figure S1) at room temperature under a high hydrostatic stress and a high strain rate of approximately 1 s^{-1} (Figure S2 and Table S2). A series of molds was employed to gradually decrease the Cu

diameter with different true deformation strains ε of 0.5, 1.0, 1.5, 2.0, and 2.5, respectively (Figure 1a, Figure S2c).

Microstructural evolutions of the swaged Cu are shown in Figure 1b–e, Tables S3 and S4, and Figures S3–S5. During the swaging process, the initial 54 μm equiaxed coarse grains (CGs) were gradually elongated along the axial direction into superlong columnar grains with an average diameter of 2.06 μm and a length of 339 μm when $\varepsilon = 2.5$ (Figure 1b, c-1, d-1; Figure S4), as statistically measured from high-angle grain boundaries (GBs) by electron backscattering diffraction (EBSD). Moreover, The RS also introduced strong ⟨111⟩ and weak ⟨100⟩ fiber textures along the Cu axis as well as high-density dislocations (Tables S3 and S5; Figures S3 and S6). The dislocation density, estimated from EBSD average local misorientation, is about 9.19×10^{14} m^{-2} when $\varepsilon = 2.5$. Parts of dislocations self-organized into polygonized dislocation walls (i.e., so-called dislocation cell boundaries) and formed substructure or subgrains with low-angle GBs inside the elongated CG grains (Figure 1c-2, d). Statistic results measured from transmission electron microscopy (TEM) indicated that the dislocation cell has an average width of 220 nm and length of 25.1 μm (Figure S5). High-resolution TEM revealed zigzag low-angle GBs formed by polygonized dislocation walls (Figure 1e). With increasing ε, the intensities
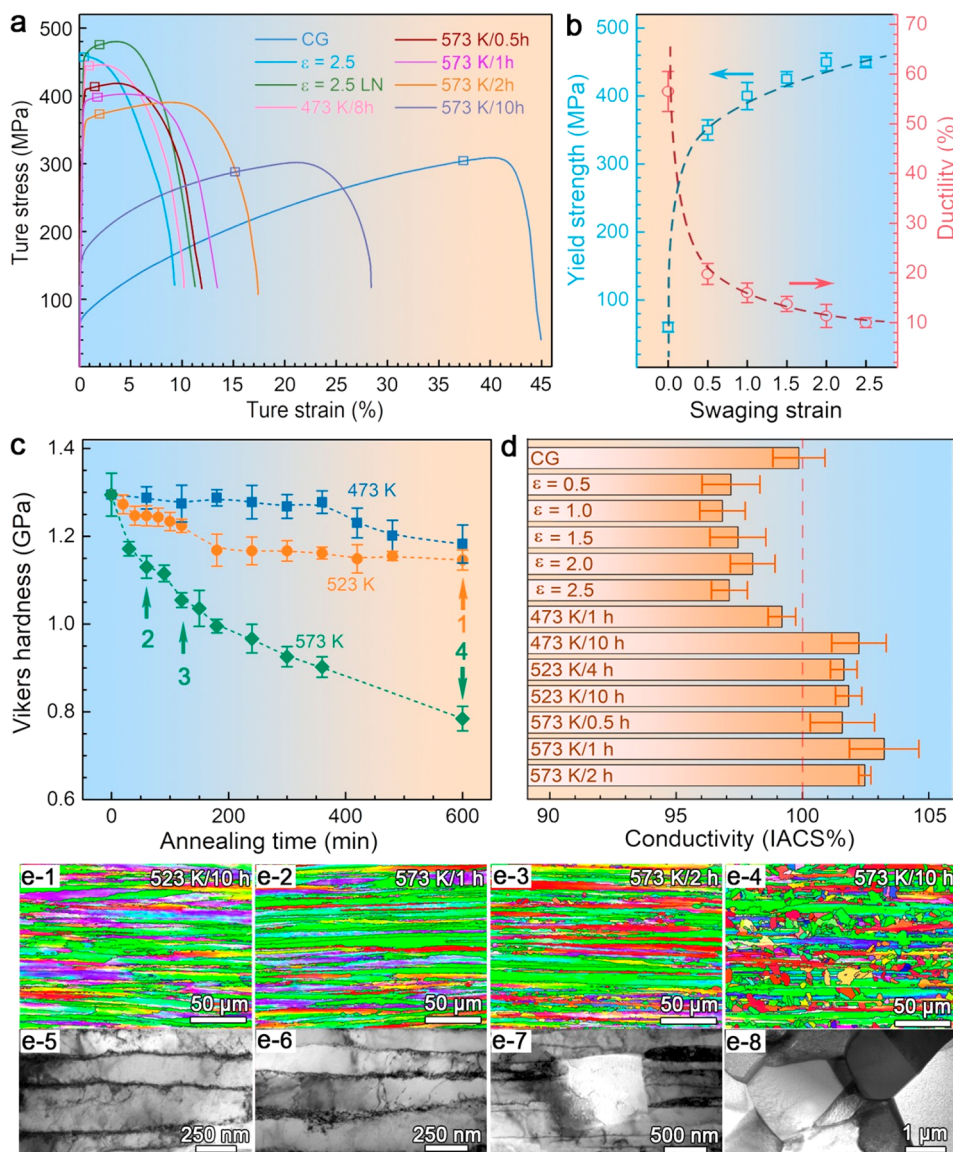
Figure 2. Mechanical, thermal, and conductive properties of the swaged Cu with ε = 2.5. (a) Quasistatic tensile curves of the swaged and CG Cu tested at room and LN temperatures. The necking onsets are marked by empty squares. (b) Yield strength and ductility (elongation to fracture) versus swaging deformation stain. (c) Microhardness evolution during the isothermal annealing process at 473, 523, and 573 K. (d) Conductivity of CG, swaged, and annealed Cu. (e) Microstructural evolutions during isothermal annealing.

of ⟨111⟩ and ⟨100⟩ textures, dislocation density, and volume fraction of low-angle GBs first increase significantly and then tend to saturate or decrease slightly when ε = 2.5.

Mechanical Properties of the Swaged Cu. Quasistatic tensile curves of the swaged Cu at room and liquid nitrogen (LN) temperatures are shown in Figures 2a and S7. The CG Cu has a yield strength of 60 MPa and tensile ductility (elongation to failure) of 57%. The swaging process gradually increases the yield strength up to 450 MPa and decreases the ductility down to 10% when ε = 2.5 (Figure 2b). For the swaged Cu, necking occurs immediately after yielding because of nearly null strain hardening capability.[10] The swaging deformation consumed the strain hardening by saturating dislocation accumulation. The ductility is enhanced to 13%, and the strain hardening as well as uniform elongation were also improved when the sample was tested at LN temperature. Moreover, annealing at 573 K for 120 min further increased the ductility up to 20% while still keeping the high yield

strength of 380 MPa. The above improved ductility and uniform elongation are due to the further enhanced dislocation accumulation capability.[10,17,18] Calculations indicated that the main strengthening mechanisms are from high-density dislocations (Calculation S1).

Thermal Stability and Conductivity of the Swaged Cu. Both isothermal and isochronal annealing were employed to characterize the thermal stability of the swaged Cu, as shown in Figures 2c, e, S7, and S8. The microhardness of the finally swaged Cu is 1.25 GPa. It keeps constant when annealed at 473 K until 400 min and slightly decreases to 1.15 GPa when annealed at 523 K for 600 min. Microstructural investigations indicated that the grain size and morphology are unchanged without any recrystallization, and the slight hardness drop is due to dislocation recovery (Figure 2e). Quantitative calculation also indicated that dislocation density is reduced by 1 order of magnitude after annealing (Table S7). An evident and rapid drop of hardness is observed when
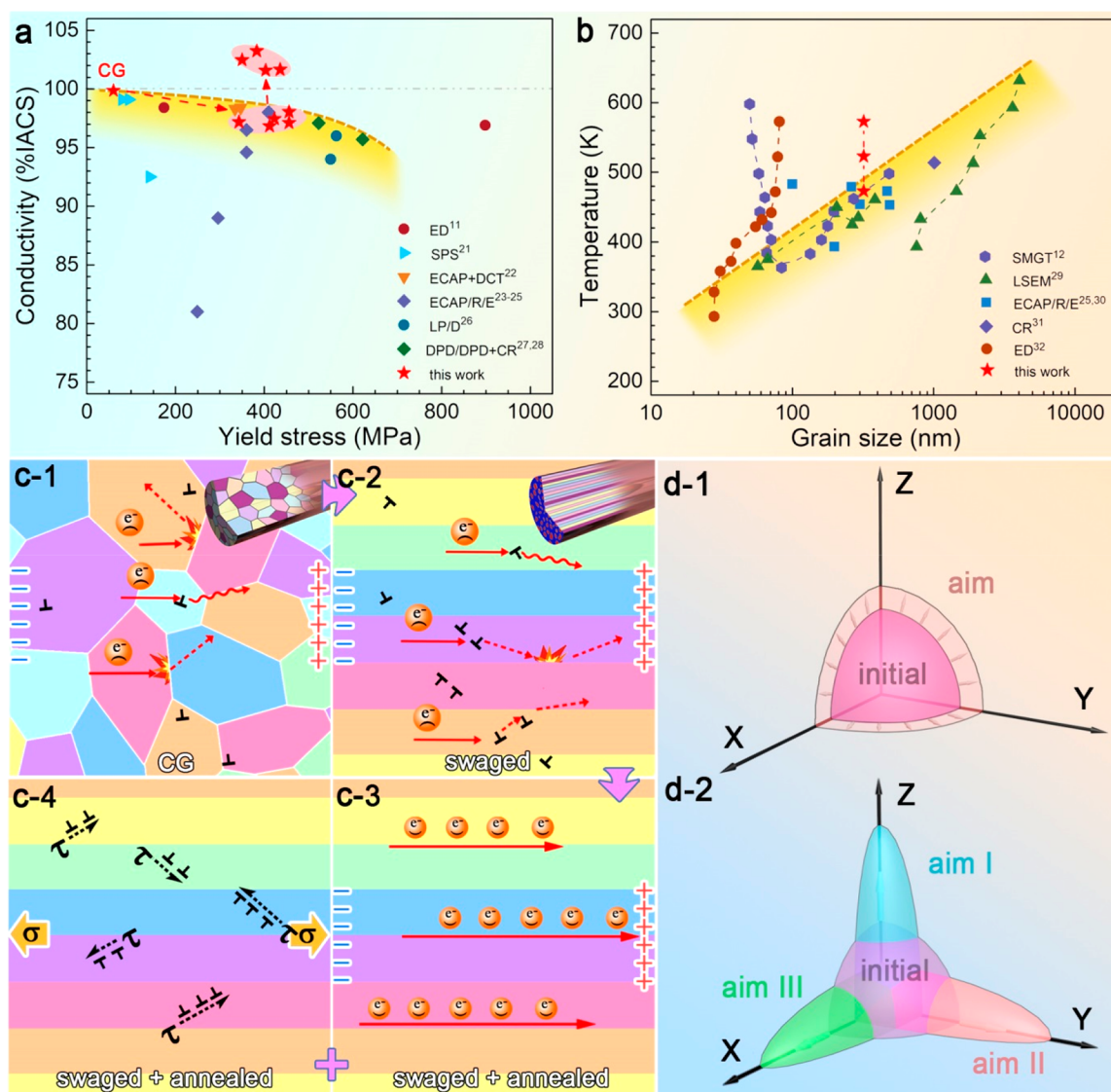
Figure 3. Literature review for relations of yield strength and conductivity/thermal stability of pure Cu prepared by different severe plastic deformation and powder sintering methods.[21−32] (a) Yield strength versus conductivity. (b) Grain size versus annealing temperature. ED, electrodeposition; SPS, spark plasma sintering; ECAP/R/E, equal-channel angular pressing/rolling/extrusion; DCT, deep cryogenic treatment; LP/D, liquid pressing/drawing; DPD, dynamic plastic deformation; CR, cold rolling; SMGT, surface mechanical grinding treatment; LSEM, large strain extrusion machining. (c) Schematic representations of microstructural evolutions of Cu during swaging and annealing processes and their influences on mechanical and conductive properties. (d) Schematic representations of traditional optimization of trade-off properties and our concept of macrodirectional design of microstructure according to the service direction.

annealed at 573 K, and the recrystallization process appears at 120 min (Figure 2e). Thermodynamic calculation indicated that the lamellar grain structure has a lower stored energy due to the lower energy and volume fraction of low-angle GBs as compared with equiaxed grains (Calculation S2).[19] Kinetic calculation revealed that the swaged Cu has higher activation energy of recrystallization (Q = 150 J/molK) as compared to equiaxed ultrafine grained Cu[20] (72 J/molK) (Calculation S3), which enhances thermal stability by retarding the recrystallization process.

Four-point probe resistivity test at room temperature indicated that the swaging process lowers the electrical conductivity of CG Cu from approximately 100 to 97% international annealed copper standard (IACS), as shown in Figure 2d. It is surprising that annealing before recrystallization increases the conductivity of the swaged Cu over that of the CG Cu and up to a highest value of 103% IACS while still

keeping the yield strength above 380 MPa. Further calculation indicates that the decreased conductivity of the swaged Cu is due to the introduction of high-density dislocations which scatter free electrons. The enhanced conductivity of the annealed Cu was caused by significantly reduced high-angle GB fraction along the conductive path (Calculation S4).

DISCUSSION

Figure 3a, b compares our results with literature data. Yield strength and conductivity of Cu are always trade-offs with each other, as shown by the dashed orange line for guidance.[21−32] An exceptional data point (red circle) with a high yield strength of 980 MPa and conductivity of 97% IACS was obtained in nanotwinned Cu[11] and basically follows the trade-off rule because twin boundaries (TBs) still have a low electron scattering effect.[33] The underlying mechanism for trade-off is

that GBs and dislocations for strengthening unavoidably introduced the lattice imperfections and caused electron scattering. It seems that the conductivity of the CG Cu is an insurmountable limit, which was broken by our data points. Strength and thermal stability of Cu are also consuming each other, as shown by the dashed orange line in Figure 3b. The final grain size increases linearly with increasing annealing temperature[12,19,20,27−31,34,35] because both GBs and dislocations for strengthening simultaneously provide a driving force for GB migration. Our data accompanied by two exceptional cases for the nanotwinned[36] and nanostructured Cu[12] deviated from the general rule and exhibited high thermal stability.

Figure 3c schematically illustrates microstructural evolutions of Cu during swaging and annealing processes and their influences on mechanical and conductive properties. For the CG Cu, high-angle GBs are the main lattice imperfections that influence conductivity (Figure 3c-1).[37] Rotary swaging simultaneously introduced the superlong grains along the Cu wire axis and high density of dislocations in grain interiors. Although the superlong grains enhanced conductivity along the axis by reducing the fraction of high-angle GBs, the high density of dislocations on the electron passageway still lowers the conductivity down to about 97% IACS (Figure 3c-2). Annealing prior to recrystallization swept away most dislocations on the electron passageway and enhanced the conductivity to over 100% IACS (Figure 3c-3). Finally, the low-angle GBs with submicrometer interval increase the yield strength via effectively blocking dislocation slip in the radial direction (Figure 3c-4).

Different from the traditional concepts of bimodal or heterogeneous composite in the literature (Figure 3d-1), our concept aims to make macrodirectional design of microstructure according to the specific working direction so that the performance of the material can be fully used, as schematically shown in Figure 3d-2. Our concept can be used to solve the other paradoxes of material properties. For battery, thermoelectric, catalytic, etc. functional and structural materials, we can design their microstructures purposefully according to the macro working directions of charge and discharge, heat conduction and conduction, reaction and loading, respectively. Obviously, we have not changed the laws of nature of material property paradox. The excellent properties in one direction come at the expense of the properties in the other direction (Figure 3d-2). This tells us that we do not have to spend our energy to make perfect materials in all aspects, but to use steel on the blade. Finally, the macrodesign of microstructure (including grain size, morphology and orientation, etc.) can be further expanded into the macrodesign of composition (different elements), phase[38] (different structures as face-centered cubic, body-center cubic, and hexagonal-close packed), etc. In this respect, gradient materials[39] and hierarchical microstructures[40] can also be classified into this category.

CONCLUSIONS

In brief, we proposed a concept of macrodirectional design of materials' microstructure based on their specific service conditions. We further prepared a Cu wire with superlong grains along the wire axis by rotary swaging, which exhibited excellent thermal stability and high strength. IACS conductivity of 103% was achieved by subsequent annealing accompanied by the yield strength above 380 MPa. Our work

provides an alternative solution for the property trade-off paradox.

METHODS

Materials and Rotary Swaging and Annealing Processes. Fiber-textured ultrafine grained Cu rods with a purity of 99.98% were synthesized by means of rotary swaging at room temperature. The as-received Cu rods with a dimension of Ø30 mm × 2000 mm were first annealed at 973 K for 2 h under Ar atmosphere to produce a coarse-grained initial microstructure with an average grain size of ∼54 μm and free of texture. The annealed Cu bars were then rotary swaged at room temperature down to Ø23.4, 18.2, 14.2, 11.1, and 8.6 mm without intermediate annealing that corresponds to true deformation degrees $\varphi(= \ln(A_0/A)$, where A_0 and A are the initial and final cross-sectional areas) of 0.5, 1.0, 1.5, 2.0, and 2.5, respectively. During swaging, four dies were first utilized to arrange uniformly in the circumference of the Cu rod; then, high speed rotation was performed around the Cu rod, and high frequency short-range strokes were simultaneously made along the radial direction. The subsequent annealing process was performed in a furnace with N_2 gas as protecting atmosphere at 473, 523, 573, 623, and 673 K, respectively. As a result, we deformed the Cu rod.

Quasistatic Uniaxial Tensile Test. Uniaxial tensile tests were performed using a LFM 20 kN (walter+bai, Switzerland) tester with a strain rate of 1×10^{-3} s^{-1} at room and liquid-nitrogen temperatures. The dog-bone-shaped tensile specimens with dimensions of $1 \times 3 \times 20$ mm^3 were cut from the central position of swaged rods with gauge length along the swaging direction. Samples were clamped by hydraulic grips to avoid slippage during the test. The strain was measured by using a standard noncontacting video extensometer. Three tensile specimens were tested to obtain reliable results.

Vickers Microhardness Test. Vickers microhardness tests were performed using an HMV-G 21DT (Shimazdu, Japan) tester with a load of 0.98 N and a dwell time of 15 s. The sample surface was mechanically polished to be fresh, and ten indentations were tested to obtain reliable results.

Electrical Conductivity Test. The electrical conductivity test was performed using a four-point probe resistivity tester at 20 °C. The specimen has a dimension of $1 \times 1 \times 52$ mm^3 with longitudinal direction parallel to the swaging direction. The value of conductivity δ is determined as follows:

$$\delta = \frac{1}{\rho} = \frac{RS}{L} \tag{1}$$

where ρ is the electrical resistivity, R is the resistance, S is the cross-sectional area, and L is the length between two voltage probes.

Microstructure Observations. X-ray diffraction (XRD) measurements were performed on a Bruker-AXS D8 diffractometer with Cu Kα radiation. The 2θ angle ranged from 40 to 100°, and the scanning speed was 6° min^{-1}.

EBSD analysis was performed on a Zeiss Auriga focused ion beam/scanning electron microscope equipped with a fully automatic Oxford Instruments Aztec 2.0 EBSD system (Channel 5 Software). EBSD sample surfaces were ground to a mirror-like condition and then electropolished using 2.1 V dc in 85% H_3PO_4 + 15% deionized water to remove micro-scratches and relax strained layers. The scanning step size and accelerating voltage were 200 nm and 15 kV, respectively.

The microstructures of the swaged Cu before and after annealing were examined by a TECNAI G2 20 LaB6 TEM instrument operating at 200 kV. TEM foils were sliced by an electrical spark machine, mechanically polished to a final thickness of about 40 μm, and then thinned by twin-jet polishing in an electrolyte of phosphoric acid (25%), alcohol (25%), and deionized water (50%) at about −10 °C. High-resolution TEM was conducted using a Titan G2 60-300 microscope that was operated at 300 kV.

ASSOCIATED CONTENT

Supporting Information

The Supporting Information is available free of charge at https://pubs.acs.org/doi/10.1021/acs.nanolett.1c00451.

Materials and methods; chemical compositions; microstructures; swaging process; list of swaging parameters; EBSD crystal orientation IPF maps, inverse pole figures, and local misorientation maps; EBSD GB maps, deformed, substructured, recrystallized grain maps, GB misorientation angle distributions, and local misorientation distributions; EDSD microstructural parameters; statistical charts; lists of θ_{KAM} and dislocation density; XRD profiles and normalized peak intensities; additional calculations; contributions of different strengthening mechanisms; isochronal annealing; EBSD crystal orientation IPF maps; dislocation densities (PDF)

AUTHOR INFORMATION

Corresponding Author

Yonghao Zhao − *Nano and Heterogeneous Materials Center, School of Materials Science and Engineering, Nanjing University of Science and Technology, 210094 Nanjing, P.R. China;* ⓞ orcid.org/0000-0002-2462-6003;
Email: yhzhao@njust.edu.cn

Authors

Qingzhong Mao − *Nano and Heterogeneous Materials Center, School of Materials Science and Engineering, Nanjing University of Science and Technology, 210094 Nanjing, P.R. China*

Yusheng Zhang − *Xi'an Rare Metal Materials Institute Co. Ltd, 710016 Xi'an, P.R. China*

Jizi Liu − *Nano and Heterogeneous Materials Center, School of Materials Science and Engineering, Nanjing University of Science and Technology, 210094 Nanjing, P.R. China*

Complete contact information is available at:
https://pubs.acs.org/10.1021/acs.nanolett.1c00451

Author Contributions

Conceptualization, Y.H. Zhao; methodology, resources, and material preparation, Q.Z. Mao; investigation and microstructural characterization, Q.Z. Mao, Y.S. Zhang, J.Z. Liu; data curation, Q.Z. Mao; writing, supervision, project administration, and funding acquisition, Y.H. Zhao. All authors have read and agreed to the published version of the manuscript.

Notes

The authors declare no competing financial interest.

ACKNOWLEDGMENTS

REFERENCES

(1) Saito, T.; Furuta, T.; Hwang, J. H.; Kuramoto, S.; Nishino, K.; Suzuki, N.; Chen, R.; Yamada, A.; Ito, K.; Seno, Y.; Nonaka, T.; Ikehata, H.; Nagasako, N.; Iwamoto, C.; Ikuhara, Y.; Sakuma, T. Multifunctional alloys obtained via a dislocation-free plastic deformation mechanism. *Science* **2003**, *300*, 464−467.

(2) Liu, H.; Zhu, Z.; Yan, Q.; Yu, S.; He, X.; Chen, Y.; Zhang, R.; Ma, L.; Liu, T.; Li, M.; Lin, R.; Chen, Y.; Li, Y.; Xing, X.; Choi, Y.; Gao, L.; Cho, H. S.; An, K.; Feng, J.; Kostecki, R.; Amine, K.; Wu, T.; Lu, J.; Xin, H. L.; Ong, S. P.; Liu, P. A disordered rock salt anode for fast-charging lithium-ion batteries. *Nature* **2020**, *585*, 63−67.

(3) Snyder, G. J.; Toberer, E. S. Complex thermoelectric materials. *Nat. Mater.* **2008**, *7*, 105−114.

(4) Ploehn, H. J. Materials science: Composite for energy storage takes the heat. *Nature* **2015**, *523*, 536−537.

(5) Coey, J. M. D. Perspective and Prospects for Rare Earth Permanent Magnets. *Engineering* **2020**, *6*, 119−131.

(6) Shen, K.; Zhang, L.; Chen, X.; Liu, L.; Zhang, D.; Han, Y.; Chen, J.; Long, J.; Luque, R.; Li, Y.; Chen, B. Ordered macro-microporous metal-organic framework single crystals. *Science* **2018**, *359*, 206−210.

(7) Mandal, P.; Pitcher, M. J.; Alaria, J.; Niu, H.; Borisov, P.; Stamenov, P.; Claridge, J. B.; Rosseinsky, M. J. Designing switchable polarization and magnetization at room temperature in an oxide. *Nature* **2015**, *525*, 363−366.

(8) Zhang, L.; Zhou, Y.; Guo, L.; Zhao, W.; Barnes, A.; Zhang, H. T.; Eaton, C.; Zheng, Y.; Brahlek, M.; Haneef, H. F.; Podraza, N. J.; Chan, M. H.; Gopalan, V.; Rabe, K. M.; Engel-Herbert, R. Correlated metals as transparent conductors. *Nat. Mater.* **2016**, *15*, 204−210.

(9) Tanaka, Y.; Himuro, Y.; Kainuma, R.; Sutou, Y.; Omori, T.; Ishida, K. Ferrous polycrystalline shape-memory alloy showing huge superelasticity. *Science* **2010**, *327*, 1488−1490.

(10) Wang, Y.; Chen, M.; Zhou, F.; Ma, E. High tensile ductility in a nanostructured metal. *Nature* **2002**, *419*, 912−915.

(11) Lu, L.; Shen, Y.; Chen, X.; Qian, L.; Lu, K. Ultrahigh strength and high electrical conductivity in copper. *Science* **2004**, *304*, 422−426.

(12) Zhou, X.; Li, X. Y.; Lu, K. Enhanced thermal stability of nanograined metals below a critical grain size. *Science* **2018**, *360*, 526−530.

(13) Zhu, Y.; Ameyama, K.; Anderson, P. M.; Beyerlein, I. J.; Gao, H.; Kim, H. S.; Lavernia, E.; Mathaudhu, S.; Mughrabi, H.; Ritchie, R. O.; Tsuji, N.; Zhang, X.; Wu, X. Heterostructured materials: superior properties from hetero-zone interaction. *Mater. Res. Lett.* **2021**, *9*, 1−31.

(14) Biswas, K.; He, J.; Blum, I. D.; Wu, C. I.; Hogan, T. P.; Seidman, D. N.; Dravid, V. P.; Kanatzidis, M. G. High-performance bulk thermoelectrics with all-scale hierarchical architectures. *Nature* **2012**, *489*, 414−418.

(15) Wegst, U. G. K.; Ashby, M. F. The mechanical efficiency of natural materials. *Philos. Mag.* **2004**, *84*, 2167−2186.

(16) Meyers, M. A.; Chen, P.-Y.; Lin, A. Y.-M.; Seki, Y. Biological materials: Structure and mechanical properties. *Prog. Mater. Sci.* **2008**, *53*, 1−206.

(17) Wang, Y. M.; Ma, E.; Valiev, R. Z.; Zhu, Y. T. Tough Nanostructured Metals at Cryogenic Temperatures. *Adv. Mater.* **2004**, *16*, 328−331.

(18) Huang, X.; Hansen, N.; Tsuji, N. Hardening by annealing and softening by deformation in nanostructured metals. *Science* **2006**, *312*, 249−251.

(19) Liang, N. N.; Zhao, Y. H.; Li, Y.; Topping, T.; Zhu, Y. T.; Valiev, R. Z.; Lavernia, E. J. Influence of microstructure on thermal stability of ultrafine-grained Cu processed by equal channel angular pressing. *J. Mater. Sci.* **2018**, *53*, 13173−13185.

(20) Jenei, P.; Gubicza, J.; Yoon, E. Y.; Kim, H. S.; Lábár, J. L. High temperature thermal stability of pure copper and copper−carbon nanotube composites consolidated by High Pressure Torsion. *Composites, Part A* **2013**, *51*, 71−79.

(21) Jiang, R.; Zhou, X.; Fang, Q.; Liu, Z. Copper−graphene bulk composites with homogeneous graphene dispersion and enhanced mechanical properties. *Mater. Sci. Eng., A* **2016**, *654*, 124−130.

(22) Wei, K. X.; Chu, Z. Q.; Wei, W.; Du, Q. B.; Alexandrov, I. V.; Hu, J. Effect of deep cryogenic treatment on microstructure and properties of pure copper processed by equal channel angular pressing. *Adv. Eng. Mater.* **2019**, *21*, 1801372.

(23) Habibi, A.; Ketabchi, M. Enhanced properties of nano-grained pure copper by equal channel angular rolling and post-annealing. *Mater. Eng.* **2012**, *34*, 483−487.

(24) Habibi, A.; Ketabchi, M.; Eskandarzadeh, M. Nano-grained pure copper with high-strength and high-conductivity produced by equal channel angular rolling process. *J. Mater. Process. Technol.* **2011**, *211*, 1085−1090.

(25) Higuera-Cobos, O. F.; Cabrera, J. M. Mechanical, micro-structural and electrical evolution of commercially pure copper processed by equal channel angular extrusion. *Mater. Sci. Eng., A* **2013**, *571*, 103−114.

(26) Han, K.; Walsh, R. P.; Ishmaku, A.; Toplosky, V.; Brandao, L.; Embury, J. D. High strength and high electrical conductivity bulk Cu. *Philos. Mag.* **2004**, *84*, 3705−3716.

(27) Zhang, Y.; Li, Y. S.; Tao, N. R.; Lu, K. High strength and high electrical conductivity in bulk nanograined Cu embedded with nanoscale twins. *Appl. Phys. Lett.* **2007**, *91*, 211901.

(28) Zhang, Y.; Tao, N. R.; Lu, K. Mechanical properties and rolling behaviors of nano-grained copper with embedded nano-twin bundles. *Acta Mater.* **2008**, *56*, 2429−2440.

(29) Wu, B.; Chen, B.; Zou, Z.; Liao, S.; Deng, W. Thermal stability of ultrafine grained pure copper prepared by large strain extrusion machining. *Metals* **2018**, *8*, 381.

(30) Zhang, Y.; Wang, J. T.; Cheng, C.; Liu, J. Stored energy and recrystallization temperature in high purity copper after equal channel angular pressing. *J. Mater. Sci.* **2008**, *43*, 7326−7330.

(31) Kumpmann, A.; Gunther, B.; Kunze, H.-D. Thermal stability of ultrafine-grained metals and alloys. *Mater. Sci. Eng., A* **1993**, *168*, 165−169.

(32) Lu, L.; Tao, N. R.; Wang, L. B.; Ding, B. Z.; Lu, K. Grain growth and strain release in nanocrystalline copper. *J. Appl. Phys.* **2001**, *89*, 6408−6414.

(33) Andrews, P. V.; West, M. B.; Robeson, C. R. The effect of grain boundaries on the electrical resistivity of polycrystalline copper and aluminium. *Philos. Mag.* **1969**, *19*, 887−898.

(34) Saldana, C.; King, A. H.; Chandrasekar, S. Thermal stability and strength of deformation microstructures in pure copper. *Acta Mater.* **2012**, *60*, 4107−4116.

(35) Mao, Z. N.; Gu, R. C.; Liu, F.; Liu, Y.; Liao, X. Z.; Wang, J. T. Effect of equal channel angular pressing on the thermal-annealing-induced microstructure and texture evolution of cold-rolled copper. *Mater. Sci. Eng., A* **2016**, *674*, 186−192.

(36) Liu, X. C.; Zhang, H. W.; Lu, K. Strain-induced ultrahard and ultrastable nanolaminated structure in nickel. *Science* **2013**, *342*, 337−340.

(37) Kim, T. H.; Zhang, X. G.; Nicholson, D. M.; Evans, B. M.; Kulkarni, N. S.; Radhakrishnan, B.; Kenik, E. A.; Li, A. P. Large discrete resistance jump at grain boundary in copper nanowire. *Nano Lett.* **2010**, *10*, 3096−3100.

(38) Ding, C. G.; Xu, J.; Shan, D. B.; Guo, B.; Langdon, T. G. Sustainable fabrication of Cu/Nb composites with continuous laminated structure to achieve ultrahigh strength and excellent electrical conductivity. *Composites, Part B* **2021**, *211*, 108662.

(39) Fang, T. H.; Li, W. L.; Tao, N. R.; Lu, K. Revealing extraordinary intrinsic tensile plasticity in gradient nano-grained copper. *Science* **2011**, *331*, 1587−1590.

(40) Liddicoat, P. V.; Liao, X.-Z.; Zhao, Y.; Zhu, Y.; Murashkin, M. Y.; Lavernia, E. J.; Valiev, R. Z.; Ringer, S. P. Nanostructural hierarchy increases the strength of aluminium alloys. *Nat. Commun.* **2010**, *1*, 63.